PHYSICAL REVIEW RESEARCH **4**, 043132 (2022)

# Time-correlated photons from an $In_{0.5}Ga_{0.5}P$ photonic crystal cavity on a silicon chip

Alexandre Chopin,[1,2] Inès Ghorbel,[1] Sylvain Combrié,[1] Gabriel Marty,[1,2] Fabrice Raineri,[2,3,*] and Alfredo De Rossi[1,†]
[1]*Thales Research and Technology, Campus Polytechnique, 1 avenue Augustin Fresnel, 91767 Palaiseau, France*
[2]*Centre de Nanosciences et de Nanotetchnologies, CNRS, Université Paris Saclay, Palaiseau, France*
[3]*Université Côte d'Azur, Institut de Physique de Nice, CNRS-UMR 7010, Sophia Antipolis, France*

(Received 19 February 2022; accepted 1 July 2022; published 23 November 2022)

Time-correlated photon pairs are generated by triply resonant four-wave-mixing in an $In_{0.5}Ga_{0.5}P$ photonic crystal cavity. Maximal efficiency is reached by actively compensating for the residual spectral misalignment of the cavity modes. The generation rate reaches 5 MHz in cavities with a $Q$-factor $\approx 4 \times 10^4$, more than one order of magnitude larger than what is measured using ring resonators with similar $Q$ factors fabricated on the same chip. The photonic crystal source is integrated on a Si photonic circuit, an important asset for applications in quantum technologies.

DOI: 10.1103/PhysRevResearch.4.043132

## I. INTRODUCTION

Parametric downconversion, either through a second-order or a third-order nonlinear optical process, underlies the emission of correlated photon pairs, entanglement [1], and squeezing. The miniaturization and the integration of sources based on these processes play an essential role in quantum technologies [2]. Maximizing the efficiency of the parametric interaction implies an improved generation rate, entanglement, antibunching, and the decrease of the pump power level [3,4]. Ultimate efficiency (i.e., single-photon nonlinearity) leads to deterministic quantum gates [5]. Considering resonantly enhanced pair generation through spontaneous four-wave mixing (SFWM), its rate $R$ depends [6] on the Kerr nonlinear index $n_2$, on the $Q$-factor of the resonances, on the effective volume for the nonlinear interaction $V_\chi$ [7], and on the pump power $P$ delivered to the resonator, namely

$$R \propto n_2^2 \frac{Q^3}{V_\chi^2} P^2. \qquad (1)$$

Therefore, the rate can be enhanced by design (increasing $Q$, decreasing the size of the resonator) or by choosing a material with a larger $n_2$. Ring resonators made of AlGaAs, a group III-V semiconductor with sizable Kerr nonlinearity, have achieved a high (MHz) internal generation rate with 10 $\mu$W on-chip pump [3]. On the other hand, due to scattering at sidewalls, the radius of high-$Q$ rings made of semiconductors is hardly smaller than 10 $\mu$m. In contrast, high-$Q$ photonic crystal (PhC) resonators with a similar $Q$-factor confine the field in a volume that is orders of magnitude smaller [8], thereby raising high expectations for a very strong nonlinear interaction. Yet, efficiency is reached only when the interacting "pump", "signal," and "idler" fields are simultaneously on resonance with the corresponding cavity modes. This condition, trivially satisfied in ring resonators, is extremely challenging in PhC. Triply resonant SFWM was reported in a multimode resonator made of three coupled single-mode PhC cavities [9]. The normalized spontaneous generation rate (300 MHz $mW^{-2}$) is large, considering the moderate $Q$-factor ($\approx 5 \times 10^3$), due to the small volume of the resonator. Correlated photon pairs have been reported in PhC waveguides [10] and coupled cavities resonator waveguides [11], both with a pulsed pump and a peak power level well above 100 mW.

A novel tuning technique, exploiting the inhomogeneous thermo-optic effect, has enabled triply resonant four-wave-mixing (FWM) in multimode high-$Q$ ($Q > 10^5$) PhC, ultimately leading to the PhC optical parametric oscillator [7]. We show that this approach, here modified to operate with a fixed wavelength pump, enables time-correlated pairs emitted at maximal efficiency (i.e., following the $Q^3$ scaling) within a PhC resonator, integrated with a silicon photonic circuit.

## II. PHOTONIC CRYSTAL SOURCE

The nanobeam PhC cavity [12] is made of $In_{0.5}Ga_{0.5}P$, a group III-V semiconductor alloy grown lattice-matched to GaAs. Its electronic band gap (1.89 eV) is large enough to suppress two-photon-absorption (TPA) of a pump in the Telecom spectral range [13]. Thus, large electric fields can be established, enabling the observation of temporal solitons at chip scale [14]. Moreover, the residual linear absorption rate is about $1.5 \times 10^{-8}$ $s^{-1}$, which is extremely small, compared to other direct gap semiconductors [15]. The period of the holes is tapered to establish an effective harmonic potential for the field, involving nominally spectrally equispaced resonances at frequencies ($\omega_-$, $\omega_0$, $\omega_+$) [Fig. 1(a)]. The PhC is coupled through an evanescent field to an underlying silicon photonic

---

[*] fabrice.raineri@inphyni.cnrs.fr

[†] alfredo.derossi@thalesgroup.com

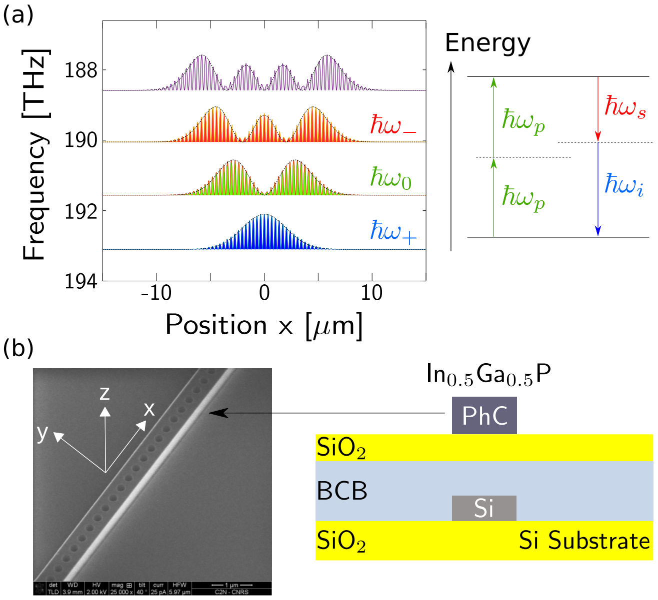

FIG. 1. Parametric PhC source. (a) Squared fields (calculated) of the first four modes (filled curves) of the PhC cavity and their envelopes (dashed lines) along the axis $x$, with $x = 0$ the center of the beam; pump ($\omega_p$), signal ($\omega_s$), and idler ($\omega_i$) photons are resonant with modes $\omega_0$, $\omega_-$, $\omega_+$ in the SFWM process. (b) SEM image of the $In_{0.5}Ga_{0.5}P$ PhC resonator on the silica layer (left) and representation of the hybrid III-V PhC on a silicon layer stack (right). BCB denotes benzocyclobutene.

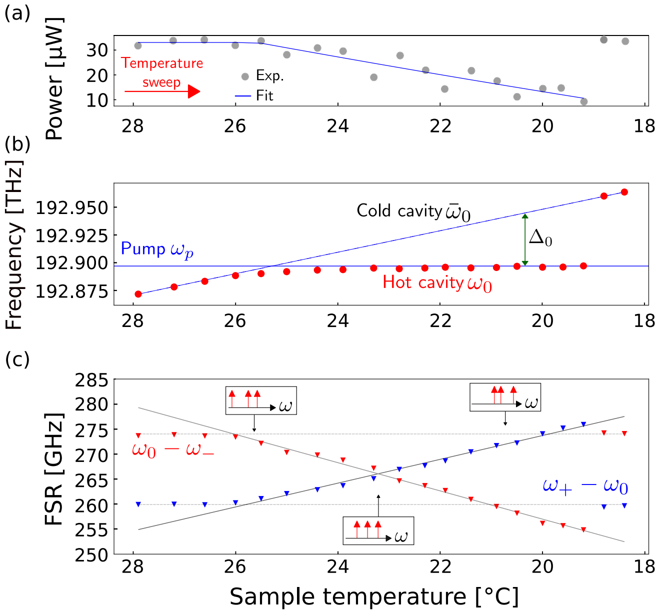

FIG. 2. Achievement of equispaced resonances through thermal sweep and fixed pump wavelength. (a) Transmitted pump, after waveguide couplers (circles; the line is a guide for the eyes) as the sample temperature is decreased. (b) Corresponding resonance frequency $\omega_0$ (circles); solid and dashed lines represent the pump $\omega_p$ and the thermo-optic drift of $\bar{\omega}_0$, respectively. (c) Corresponding measured FSR (markers), fit (solid lines), and value at uniform temperature (dashed lines); insets represent the aligned/not aligned configurations.

wire [Fig. 1(b)]. The full details on the fabrication and FWM process are given in Ref. [16] and in Appendix B 1. The cavities considered hereafter have quality factors ranging from $2 \times 10^4$ to $10^5$ and resonances between 192 and 194 THz (1545–1560 nm). The same chip contains ring resonators fabricated simultaneously with the PhC resonators, with a radius of 30 $\mu$m and comparable $Q$ factors.

Compared to SFWM in a ring resonator, a specific feature here is the tuning process and the dependence of the emission rate on the injected pump power and the detuning. This stems from the markedly inhomogeneous and only partially overlapped distribution of the field of the interacting modes. Consequently [7], when the cavity heats up due to pump dissipation, the modes experience a differential thermorefractive effect, which compensates for the unavoidable fabrication tolerances. This differential effect depends on the heat diffusion length [17], hence on the thermal conductivity, and on the spatial profile of the modes. The pump laser is operated at a fixed frequency $\omega_p$, larger than the $\overline{\omega}_0$ resonance at a sample temperature $T = 28\,^\circ$C. Hereafter, the overline denotes the absence of internal dissipation, hence homogeneous temperature in the sample. The transmission decreases as the temperature is decreased below $T = 26\,^\circ$C, until the bistable jump is reached at $T = 19\,^\circ$C [Fig. 2(a)]. Optical coherent tomography (OCT) is used to track the corresponding thermal drift of the resonances (see Appendix B 3). This is shown in Fig. 2(b). As $\omega_0$ approaches the pump $\omega_p$, the energy stored in the mode, and hence the internal dissipation, increase and $\omega_0$ is clamped to the pump (within $T = 26$–$19\,^\circ$C); the drift $\omega_0 - \bar{\omega}_0$ is linearly related to the sample temperature, and it can be approximated by the pump offset $\Delta_0 = \omega_p - \bar{\omega}_0 \approx \omega_0 - \bar{\omega}_0$. The differential thermo-optic effect is apparent in Fig. 2(c), as the intervals $\Delta\omega_\pm = |\omega_\pm - \omega_0|$ change until they equalize at a given temperature (23 °C here). The corresponding pump detuning is $\Delta_{\rm opt}$, while $\Delta_{\rm bist}$ denotes the detuning at the bistable jump. Let us define the mismatch $2\mathcal{D} = \Delta\omega_+ - \Delta\omega_-$, which is zero when the modes are aligned and FWM is triply resonant. This is only possible [Fig. 2(c)] if the initial mismatch (when the temperature in the sample is uniform) is negative ($2\overline{\mathcal{D}} < 0$). This is related to the sign of the differential thermo-optic effect. If this condition is satisfied, the pump power needs only to be large enough to keep the resonance locked until triple resonance is reached.

## III. GENERATION OF CORRELATED PAIRS

The fixed pump frequency is chosen such that the signal and idler are both aligned with the channels of the DWDM (dense wavelength division multiplexing) filter at the output of the sample [Fig. 3(a)]. A band-pass (BP) filter is also used to remove the amplified spontaneous emission from the pump laser before entering the sample. The power at the input of the cavity is estimated to be $P_{c,\rm in} = 250\ \mu$W. Considering that, the 110 dB overall pump suppression at the detectors, ensured by cascading a BP filter on the signal and idler channels, is enough for our purposes. Two single-photon avalanche photodiodes (SPADs) (quantum efficiency $\eta_q = 20\%$, deadtime $\tau_D = 15\ \mu$s) are operated in gated mode (signal frequency $f = 3$ MHz, duty cycle $\sigma = 0.5$) and connected to a time

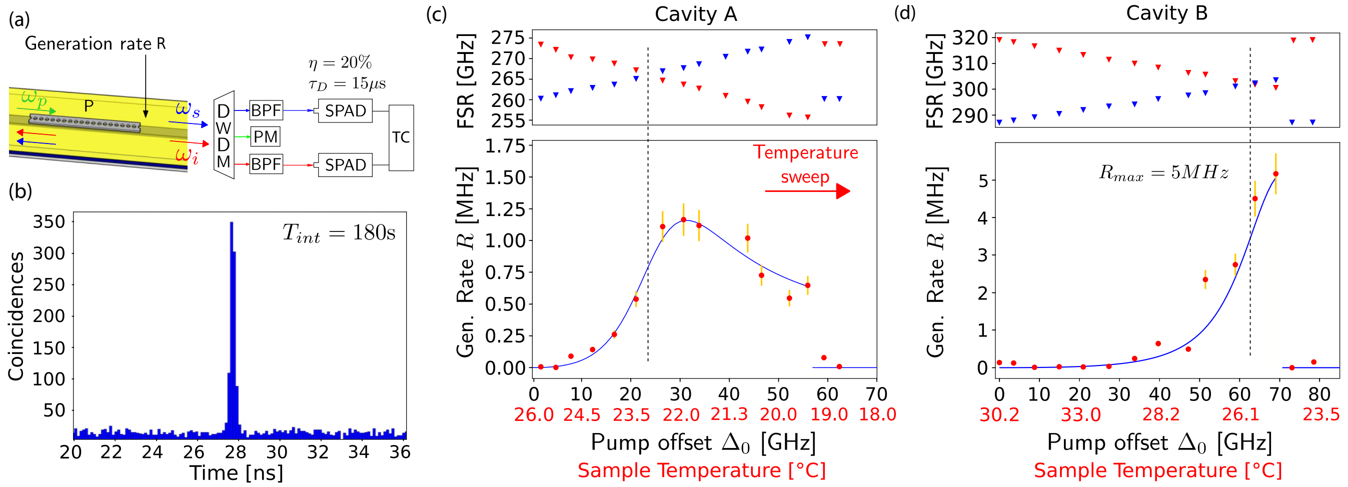

FIG. 3. Photon pairs generation in PhC. (a) Simplified time-correlation measurement setup: Dense wavelength division multiplexing (DWDM), band-pass filters (BPF), power meter (PM), single-photon avalanche photodiode (SPAD), and time correlator (TC). (b) Raw coincidence (at max. rate 5 MHz) histogram with integration time $T_{\rm int}$, time bin 90 ps. (c),(d) On-chip pair generation rate $R$ (bottom) and corresponding FSR (top) as a function of the pump offset, controlled by the temperature; symbols and error bars are experimental points, and the solid line is the theory with no fitting parameters; the vertical dashed line marks the equal FSR; (c),(d) correspond to cavities ($A$, $B$). Cavity $A$ has a lower initial mismatch $|2\overline{\mathcal{D}}|$ than cavity $B$.

correlator (TC), as shown in Fig. 3(a). The count of single photons on each channel ($N_1, N_2$) increases above the background simultaneously in both channels as the triply resonant FWM is established [see Appendix B, Fig. 7(b)].

A raw coincidences histogram, Fig. 3(b), is collected as a function of the sample temperature with integration time $T_{\rm int}$. The raw count of coincidences $C_{\rm raw}$ (the sum of all coincidences over the main peak of width $2T_j = 300$ ps, where $T_j$ is the timing jitter of the detectors) is corrected with the estimate of the accidental counts $A$ (summing over the same width outside the peak) to generate the "true" coincidences $C_T = C_{\rm raw} - A$. The coincidence to accidental ratio is $\mathrm{CAR} = C_T/A$, following Ref. [18]. To cope with the saturation of the SPADs as the count rate increases, further correction is applied and real coincidences are $C = C_T(1 - N_1\tau_D)^{-1}(1 - N_2\tau_D)^{-1}\sigma^{-1}$ [19]. Finally, the coincidence rate is then $R_{\rm det} = C/T_{\rm int}$ (for details, see Appendix B 2 f).

The on-chip pair generation rate $R$, that would be relevant, for instance, in a quantum chip, is deduced by taking into account the photon loss in the two channels $\alpha_i$ and $\alpha_s$ from the silicon wire all the way to the detectors considering their quantum efficiency [6], hence $R = R_{\rm det}/\alpha_i\alpha_s$. The attenuation ranges between 25 and 30 dB, depending on the sample. The main contributions are the tunable BP filters, the chip to fiber grating couplers, and the quantum efficiency of the SPADs. Moreover, in contrast with ring resonators, side-coupled PhCs emit signal and idler photons with equal probability in both directions of the silicon waveguide, giving an additional 3 dB loss.

Figure 3(c) shows the coincidence rate $R$ as the cavity is tuned towards its maximum efficiency by changing its baseline temperature, pump wavelength, and power being fixed. A clear maximum, sharply emerging from noise, is observed before a decrease due to a deviation from the triply resonant configuration. The sudden drop after the bistable jump clearly indicates that the system is then out of resonance. Yet, the maximum is reached after crossing the point of triple resonance, Figs. 3(c) and 3(d). This is explained by a model introduced hereafter. Starting from the connection between spontaneous and stimulated FWM [20], the spontaneous emission rate is

$$R = \int \eta_\chi d\nu, \tag{2}$$

with the probability of stimulated conversion $\eta_\chi$ integrated over all the possible combinations of signal and idler frequencies satisfying the photon energy conservation. It can be expressed in the limit of undepleted pump and low parametric gain [7]. Combining this with Eq. (2), under the approximation that the energy in the cavity scales linearly with the pump offset (true if the absorption is linear), gives (for $\Delta_0 < \Delta_{\rm bist}$)

$$R = \frac{\eta_\chi^{\max}}{4}\,\frac{\Delta_0^2}{\Delta_{\rm bist}^2}\,\frac{\Gamma_-\Gamma_+(\Gamma_- + \Gamma_+)}{(\Gamma_- + \Gamma_+)^2 + 16\overline{\mathcal{D}}^2\left(1 - \frac{\Delta_0}{\Delta_{\rm opt}}\right)^2}, \tag{3}$$

where $\eta_\chi^{\max}$ is the maximum conversion probability at a given pump power (see the definition in Appendix A), and $\Gamma_{-,0,+}$ are the total cavity damping rate. $\Delta_{\rm bist}$ is the value of $\Delta_0$ for which the bistable jump is reached, and $\Delta_{\rm opt}$ is the value at which $\mathcal{D} = 0$, i.e., the resonances are aligned exactly. Let us note that $\Delta_0^2/\Delta_{\rm bist}^2 < 1$ and is close to 1 at maximum efficiency. $\Delta_{\rm bist}$ depends on the maximum power that can be dissipated in the cavity $P$, and it is roughly proportional to the initial mismatch $\overline{\mathcal{D}}$. Details on the derivation of these formulas are given in Appendix A.

The model [Eq. (3)] is superimposed on the measurement in Fig. 3(c), with all these parameters being measured independently (see Appendix B) and none fitted. By inspecting the equation, we note that $R$ depends on $\Delta_0$ via two terms: one is maximized when $\Delta_0 = \Delta_{\rm opt}$, i.e., triply resonant FWM, and the other increases with $\Delta_0^2$. So, $R$ continues to increase, although the triple resonance is loosely satisfied

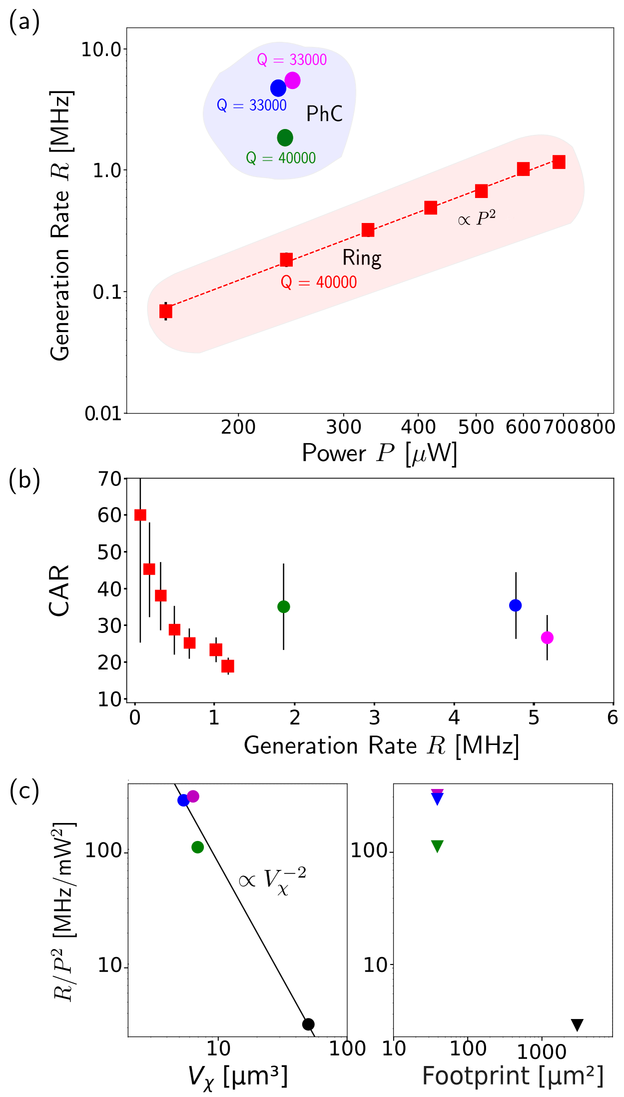

FIG. 4. SFWM in PhC (circles) and ring (squares) resonators. (a) On-chip pair generation rate vs power (markers) and $P^2$ fit (dashed line); (b) corresponding CAR vs generation rate (same color and symbol code); (c) generation rate on-chip normalized with the equivalent pump power vs the nonlinear interaction volume $V_\chi$ and the footprint of the device. Circles (squares) denote PhC (rings).

($\Delta_0 - \Delta_{\mathrm{opt}} < \Gamma$). The agreement with the experimental points is remarkable. The model predicts that the optimal choice of the pump power is such that the bistable jump occurs just a little after the triply resonant FWM. This condition is shown in Fig. 3(d) using cavity $B$, where a 5 MHz maximum on-chip generation rate is estimated with roughly the same on-chip power as cavity $A$. Crucially, it demonstrates that the device can be tuned to its maximum efficiency, which ultimately depends on the $Q$ factor.

## IV. DISCUSSION

Let us compare the PhC with an InGaP ring resonator. The radius is 30 $\mu$m, and the $Q$ factor is roughly the same as in the PhC (see Appendix C 2). As shown in Fig. 4(a), the generation rate $R$ from rings scales with the square of the pump, as expected. Yet, it is apparent that for PhC cavity made of the same material, $R$ is much larger by at least one order of magnitude when normalized to the pump power. Figure 4(b) shows that in rings, the CAR decreases with the generation rate, indicating that accidental counts are mostly due to lost pairs, hence insertion loss [18]. The corresponding measurement for PhC reveals that the generation rate $R$ is much larger at the same CAR, because of a much tighter confinement. This is apparent in Fig. 4(c), as the maximum generation rate, normalized to the equivalent pump power (see Appendix B 2 e), scales as the square of the inverse of $V_\chi$, which is an order of magnitude larger in the rings. Let us note that $V_\chi$ takes into account the spatial distribution and mutual overlap of the interacting modes, therefore it is distinct from the physical volume of the resonator; indeed, the difference in terms of footprint is even more pronounced.

Let us now compare our PhC cavity to existing resonant parametric sources made of semiconductor materials in Table I. A sizable spontaneous emission rate, but not a coincidence rate, is reported in a silicon PhC [9], due to the very small volume where parametric interaction takes place. Related to the interaction volume is the footprint, which is at least an order of magnitude smaller than in rings. We report a relatively modest CAR, which is due to large (7 dB) insertion losses in the chip to fiber coupling, limited detection efficiency, and unbalanced escape probability. All these limitations are not inherent to the PhC technology, and they can be mitigated through design optimization. InP microring resonators [23] feature a larger efficiency than our InGaP rings due to the larger nonlinearity of the material. However, their maximum measured generation rate is much smaller because of the strong saturation induced by TPA. TPA is removed in a silicon ring operated with a reverse biased *p-i-n* junction [21].

In Fig. 5 we consider the scaling of the generation efficiency $R/P^2$ with the figure of merit $M = (n_2^2 Q^3)/V^2$, which is the theoretical prediction, Eq. (1), in the limit of vanishing internal losses. This requires a correction to account for the coupling efficiency of the pump to the cavity mode. Therefore, the efficiency $R$ is recalculated by replacing the on-chip power $P_c$ with the equivalent power, which we define as that which would produce the same generation rate if the cavity had the same $Q$ factor but no internal losses. This amounts to a correction $2\kappa/\Gamma P_c = 0.514\,P_c$ (see details in Appendix B 2 e).

It is apparent that scaling is well respected by parametric photon pair generators. On the other hand, it has been shown that PhC sources can be tuned to maximum efficiency, which depends on this scaling. This legitimizes the extrapolation of the results to the case of a multimode PhC cavity with parameters extracted from existing samples, as in Ref. [24]. Here the loaded $Q$-factor is about $4 \times 10^5$, and the intrinsic one is about $7 \times 10^5$ on average. This leads to an estimate (Table I) of the efficiency of about 300 GHz/mW$^2$, which is comparable to the state-of-the-art.

## V. CONCLUSIONS

In summary, we have reported time-correlated pair generation from a PhC resonator systematically operated at its maximum efficiency, due to a thermal tuning mechanism. This only requires a fixed wavelength laser pump, removing the

TABLE I. Comparison between correlated photon pairs sources. $R_{\max}$ is the maximum measured rate. The CAR value correspond to a generation rate of 1 MHz. The brightness $B = R/(P^2 \Delta\omega)$, with $\Delta\omega$ the FWHM of the side resonances.

| Material | Geometry | $Q$ | Footprint ($\mu$m$^2$) | $R_{\max}$ (MHz) | $R/P$ (MHz/mW$^2$) | $B$ (mW$^{-2}$) | CAR at $R = 1$ MHz | Ref. |
|---|---|---|---|---|---|---|---|---|
| AlGaAs | Ring | $\mathbf{1.2 \times 10^6}$ | 608 | 10 | **20 000** | **200** | **2000** | [3] |
| Si | Ring | $3.75 \times 10^4$ | 314 | 123 | 5.3 | 0.001 | 600 | [21] |
| Si | Ring | $9.2 \times 10^4$ | 314 | 1.1 | 149 | 0.15 | 900 | [22] |
| Si | Ring | $1.5 \times 10^4$ | 314 | **27** | 6.71 | 0.00052 | 120 | [2] |
| InP | Ring | $4.3 \times 10^4$ | 1810 | 0.05 | 145 | 0.031 | <277 | [23] |
| InGaP | Ring | $4 \times 10^4$ | 2827 | 1 | 2.52 | 0.00052 | 25 | This work |
| InGaP | PhC | $4 \times 10^4$ | **50** | 5 | 80 | 0.02 | 35 | This work |
| Si | PhC | $6 \times 10^3$ | **10** | | 300 | 0.009 | | [9][a] |
| InGaP | PhC | $4 \times 10^5$ | 50 | | 300 000 | 600 | | Extrapolated |

[a] Spontaneous generation rate, no coincidences measurements.

need for a tunable source, which is convenient for integration. The amount of power to be dissipated in the cavity, in order to tune the source at its maximum efficiency, depends on the initial mismatch between the modes $\overline{\mathcal{D}}$. This means that fabrication disorder induces a variability in the performances also because of this mechanism. The agreement with theory is within experimental error, with no need for fitting parameters. Simple scaling with volume is demonstrated by comparison with a ring resonator fabricated on the same chip. Put in a broader perspective, this class of parametric sources of photons obeys the scaling rules of generation efficiency with design parameters, as ring resonators do. This implies that a sizable improvement is possible *by design*. On the other hand, these sources have a unique feature: only a very few modes (here three) are involved in the parametric interaction. This property is maintained when operating from pair generation all the way to optical parametric oscillation. Moreover, with the integration of the PhC with a photonic circuit, it is still possible to include the essential functions of pump suppression and signal/idler separation, and in perspective, to operate several of such sources simultaneously, with reduced concerns about unwanted competing parametric interactions.

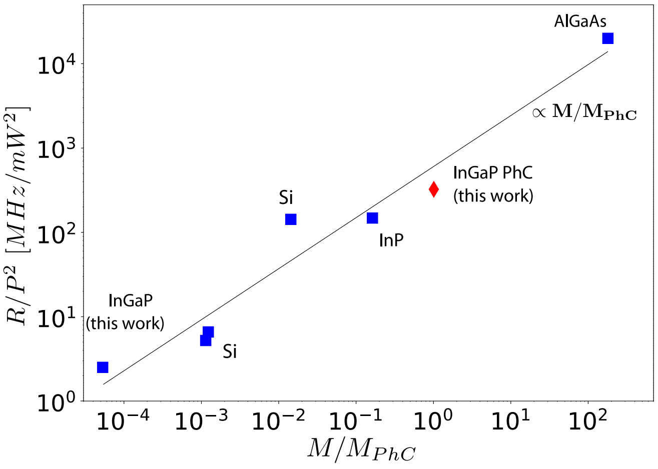

FIG. 5. Pair generation rate $R$ normalized to $P^2$ from Table I vs the scaled figure of merit $M/M_{\mathrm{PhC}}$, relative to the PhC source. The red diamond represents PhC, blue squares denote ring resonators, and the black line is a linear fit. For rings, the nonlinear volume is calculated following $V_\chi = 1.54V$, with $V$ the volume of the resonator. The Kerr nonlinear index $n_2$ is $0.6 \times 10^{-17}$ m$^2$/W for Si/InGaP, $n_2$ is $2.7 \times 10^{-17}$ m$^2$/W for InP, and $n_2$ is $4.0 \times 10^{-17}$ m$^2$/W for AlGaAs.

## ACKNOWLEDGMENTS

This work was Funded by the Agence nationale de la recherche (ANR) under the contract COLOURS (ANR-21-CE24-0024). The authors thank Grégory Moille for the design of the rings used here. Thierry Debuisschert and Kamel Bencheikh for discussions and clarifications. Laurent Labonté and Sébastien Tanzilli for having provided assistance in preliminary experiments in their facilities. The work was partly supported by the French Renatech network.

## APPENDIX A: THEORY

### 1. Triply resonant spontaneous four-wave mixing

A model is derived to account for the generation of photon pairs via spontaneous four-wave-mixing (SFWM) in photonic crystal (PhC) cavities. The conservation of the energy as each pair of pump photon is converted into idler and signal photons (hence $2\omega_p = \omega_s + \omega_i$) implies that these are placed symmetrically relative to the pump in the spectra. The probability of SFWM is maximized when the pump, signal, and idler are all in resonance with the corresponding modes of a cavity. This requires three eigenfrequencies to be strictly equally spaced. This triply resonant configuration (TRC) is rarely met in PhC, as it requires an appropriate design and then an external tuning mechanism [7] to compensate for residual misalignment due to structural disorder during fabrication. Let us label the angular frequencies of the cavity modes $\omega_-$, $\omega_0$, and $\omega_+$, and their total damping rate $\Gamma_-$, $\Gamma_0$, and $\Gamma_+$ [Fig. 6(a)]. The cavity modes are coupled to a waveguide through the rates $\kappa_-, \kappa_0, \kappa_+$. The probability of stimulated conversion efficiency is defined for both inside ($\eta_\chi^{\mathrm{int}}$) and outside ($\eta_\chi$) the cavity. The link between the internal and external efficiency can be established with the photon escape efficiency $\eta$ [25], which is calculated for a PhC resonator in [7],

$$\eta = \frac{\kappa}{\Gamma}. \tag{A1}$$

Hence a pair is emitted if both signal and idler photons escape the cavity, leading to [the signal is related to $(-)$ resonance

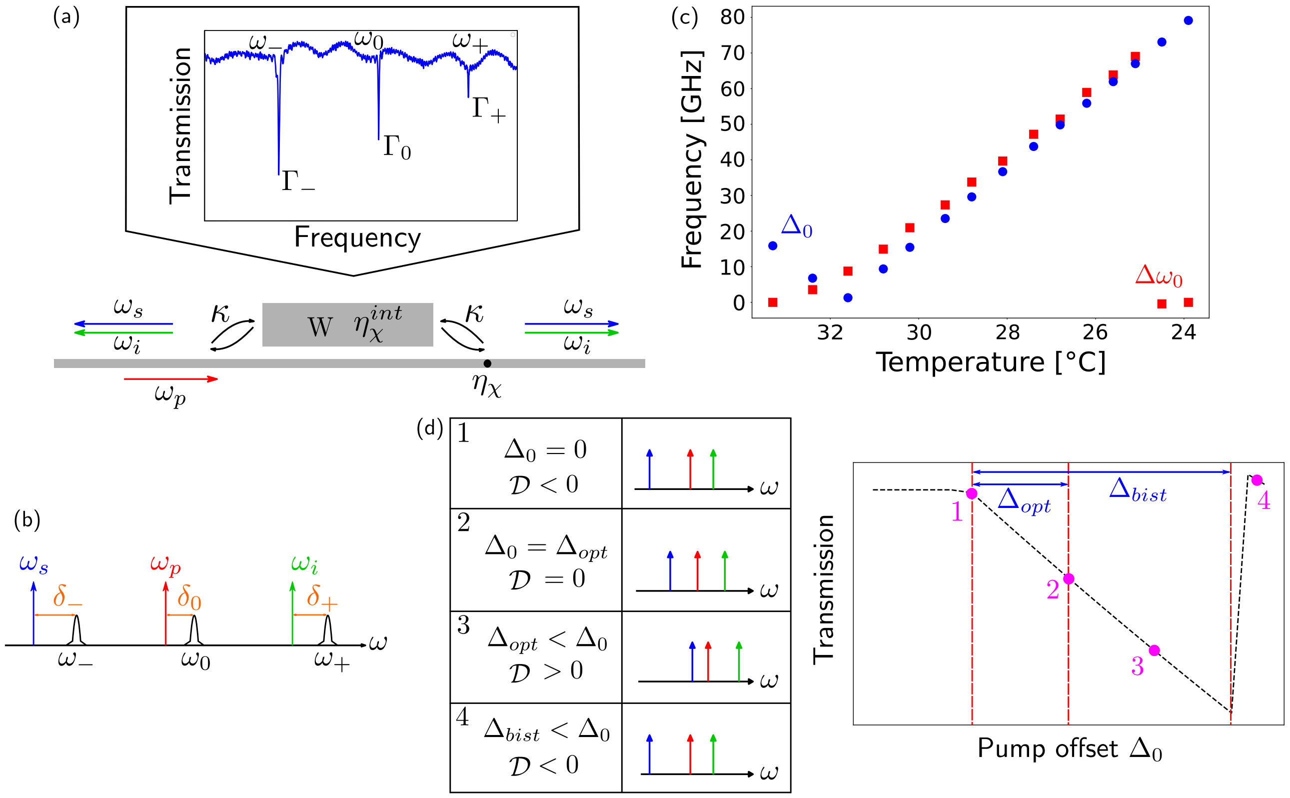

FIG. 6. Triply resonant cavity model. (a) Schematic of the system. $\omega_{p,s,i}$ are, respectively, the pump, signal, and idler angular frequencies. The cavity, whose typical spectrum shows three modes of frequencies $\omega_{-,0,+}$ and total damping rate $\Gamma_{-,0,+}$, is coupled to a waveguide through the coupling rates $\kappa_{-,0,+}$; $\eta_\chi^{\text{int}}$ ($\eta_\chi$) is the stimulated conversion efficiency inside (outside) the cavity. $W$ is the dissipated energy in the cavity. (b) Detunings $\delta$ between the modes of the cavity and the pump, signal, and idler angular frequencies. (c) Experimental evolution of the resonance shift $\Delta\omega_0$ and the pump offset $\Delta_0$ vs temperature. (d) Pump offset and frequency mismatch $\mathcal{D}$ for different operating points of the system, represented on a typical transmission spectrum. $\Delta_{\text{opt}}$ ($\Delta_{\text{bist}}$) is the value of $\Delta_0$ for which the triply resonant configuration (bistable jump) is reached.

and the idler is related to (+) resonance]

$$\eta_\chi = \eta_-\eta_+\eta_\chi^{\text{int}}. \tag{A2}$$

### 2. Definition of the detunings and frequency mismatch

As the triply resonant configuration is rarely met in PhC without an external tuning mechanism, the deviation to this operating point is expressed with two different quantities. First, the frequency detuning $\delta$ between the cavity mode frequencies and the pump, signal, and idler modes is depicted in Fig. 6(b) and defined as [7]

$$\begin{aligned}\delta_0 &= \omega_p - \omega_0,\\ \delta_- &= \omega_s - \omega_-,\\ \delta_+ &= \omega_i - \omega_+.\end{aligned} \tag{A3}$$

At the TRC, $\delta_- = \delta_0 = \delta_+ = 0$. Secondly, the free spectral range (FSR) can be expressed with the eigenfrequency mismatch $2\mathcal{D} = (\omega_+ - \omega_0) - (\omega_0 - \omega_-)$ [7]. This value is also equal to 0 at the TRC as the modes are equally spaced, i.e., $\omega_0 - \omega_- = \omega_+ - \omega_0$. In the absence of dissipation (no pump), the temperature is uniform in the sample, and we denote as $2\overline{\mathcal{D}}$ the mismatch measured under this condition. The overline will hereafter denote this condition, which we will also refer to as a "cold cavity." The mismatch can be compensated by thermal tuning only if $(\omega_0 - \omega_-) > (\omega_+ - \omega_0)$ ($2\overline{\mathcal{D}} < 0$), because of the specific dependence of the thermorefractive effect on the modes [16]. Combining Eq. (A3) and the conservation of the energy leads to

$$\delta_+ = 2\delta_0 - 2\mathcal{D} - \delta_-. \tag{A4}$$

### 3. Energy dissipation in the cavity

The tuning mechanism harnessed here stems from the nonuniform temperature profile over the sample generated by the dissipation from the pumped mode $\omega_0$. Under steady-state operation, the cavity is at a stable equilibrium point, where the cavity-laser detuning is such that energy in the cavity, hence the dissipation, is exactly what is needed to generate the required thermorefractive frequency shift. Under this condition, the energy in the cavity $W$ is proportional to the pump offset $\Delta_0 = \omega_p - \bar{\omega}_0$, as long as only linear absorption occurs [7]:

$$W = a\Delta_0. \tag{A5}$$

In our case, the pump frequency is fixed and the temperature of the sample is decreased. In the absence of a laser, the "cold" cavity resonance $\bar{\omega}_0$ frequency would be linearly shifted due to thermo-optic effects. In the presence of a pump laser, the "hot" $\omega_0$ cavity resonance will drift from the expected linear trend of $\bar{\omega}_0$ and will be clamped to $\omega_p$ [Fig. 2(b)], inducing spectral shift of the resonance $\Delta\omega_0 = \omega_0 - \bar{\omega}_0$. It can then be assumed until the bistable jump that $\omega_p \approx \omega_0$, and so

$$\Delta_0 = \omega_p - \bar{\omega}_0 \approx \omega_0 - \bar{\omega}_0 = \Delta\omega_0. \tag{A6}$$

In the following, $\Delta\omega_0$ will be approximated by the pump offset, as the latter is directly measurable; Fig. 6(c) demonstrates that this choice is sensible. The pump offset $\Delta_0$ and the resonance spectral shift $\Delta\omega_0$ are related via the pump detuning $\delta_0$ as $\Delta_0 = \Delta\omega_0 + \delta_0$. The previous formula means that $\delta_0$ can be neglected compared to other detuning terms.

Two important points of the system can be defined here. The TRC point is reached for a given value $W = W_{\text{opt}}$, also defining the corresponding value for the pump offset $W_{\text{opt}} = a\Delta_{\text{opt}}$. The bistable jump [26] occurs when the dissipated energy is maximum ($W_{\text{max}}$), corresponding to a pump offset value $\Delta_{\text{bist}}$: $W_{\text{max}} = a\Delta_{\text{bist}}$. $\Delta_{\text{bist}}$ is then directly controlled by the pump power $P$. These points and the corresponding values of $\mathcal{D}$ are shown in Fig. 6(d) on a typical transmission curve with the pump offset. It also follows that

$$\mathcal{D} = \overline{\mathcal{D}} + b\Delta_0, \tag{A7}$$

with $b$ being a coefficient.

$\mathcal{D}$ will decrease from its initial cold cavity value $\overline{\mathcal{D}}$ with a linear evolution. At the triply resonant configuration, $\mathcal{D} = 0$ and $\Delta_0 = \Delta_{\text{opt}}$. The parameter $b$ is deduced, and $\mathcal{D}$ can be rewritten,

$$\mathcal{D} = \overline{\mathcal{D}}\left(1 - \frac{\Delta_0}{\Delta_{\text{opt}}}\right). \tag{A8}$$

### 4. Expression of the stimulated conversion efficiency

Under the approximation of undepleted pump and low parametric gain [7], the stimulated conversion efficiency $\eta_\chi$ can be expressed as

$$\eta_\chi = \eta_\chi^{\text{max}} \mathcal{L}\left(\frac{2\delta_0}{\Gamma_0}\right)^2 \mathcal{L}\left(\frac{2\delta_-}{\Gamma_-}\right) \mathcal{L}\left(\frac{2\delta_+}{\Gamma_+}\right), \tag{A9}$$

where $\mathcal{L}(x) = \frac{1}{1+x^2}$ is a Lorentzian function. $\eta_\chi^{\text{max}}$ is the maximum value of $\eta_\chi$ obtained when the resonance triplet is aligned. It is directly related to the on-chip pump power $P$, the coupling, and total damping rates of the different modes as [7]

$$\eta_\chi^{\text{max}} \propto \frac{\kappa_0^2 \kappa_- \kappa_+}{\Gamma_0^4 \Gamma_-^4 \Gamma_+^2} P^2. \tag{A10}$$

The energy stored in the pump mode is

$$W = W_{\text{max}} \mathcal{L}\left(\frac{2\delta_0}{\Gamma_0}\right). \tag{A11}$$

### 5. Derivation of the pair generation rate

The internal power of spontaneous emission is related to the internal stimulated conversion efficiency as shown in [20,25] by

$$P_{\text{spont}}^{\text{int}} = \hbar\omega \int \eta_\chi^{\text{int}} d\nu, \tag{A12}$$

where $\hbar$ is the reduced Planck constant, and $\nu$ is the frequency. The internal spontaneous emission rate $R^{\text{int}}$ can be linked to the external conversion efficiency $\eta_\chi$ using (A2),

$$R^{\text{int}} = \frac{P_{\text{spont}}^{\text{int}}}{\hbar\omega} = \frac{1}{\eta_- \eta_+} \int \eta_\chi d\nu. \tag{A13}$$

Photon pair emission implies that both the signal and the idler escape from the cavity,

$$R = \eta_- \eta_+ R^{\text{int}} = \int \eta_\chi d\nu. \tag{A14}$$

Using (A4), (A9), and (A11), we obtain

$$R = \eta_\chi^{\text{max}} \left(\frac{W}{W_{\text{max}}}\right)^2 \int \mathcal{L}\left(\frac{2\delta_-}{\Gamma_-}\right) \mathcal{L}\left(\frac{4\delta_0 - 4\mathcal{D} - 2\delta_-}{\Gamma_+}\right) d\nu. \tag{A15}$$

Integration is performed with $\delta_- = 2\pi(\nu - \nu_s)$. Neglecting $\delta_0$ in the last Lorentzian (see Appendix A 3) and by injecting (A5) and (A8), we finally obtain

$$R = \frac{\eta_\chi^{\text{max}}}{4} \left(\frac{\Delta_0}{\Delta_{\text{bist}}}\right)^2 \frac{\Gamma_- \Gamma_+ (\Gamma_- + \Gamma_+)}{(\Gamma_- + \Gamma_+)^2 + 16\overline{\mathcal{D}}^2 \left(1 - \frac{\Delta_0}{\Delta_{\text{opt}}}\right)^2}. \tag{A16}$$

## APPENDIX B: EXPERIMENT

### 1. Sample fabrication

The hybrid structure is composed of an InGaP PhC cavity bonded to a silicon-on-insulator (SOI) platform using benzocyclobutene adhesive [16]. The cavity is fabricated using negative single pass e-beam lithography with hydrogen silesquioxane resist (HSQ), and it is composed of holes, which are drilled with inductive coupling plasma (ICP) and etched with an HBr/He/$O_2$ gas mix. The advantage of this platform is that it benefits from the InGaP large band gap (1.89 eV) to mitigate both nonlinear absorption (particularly two-photon absorption) and large nonlinearity $n_2$. The integration on the silicon platform is beneficial as it is widely regarded in nanophotonics, and the foundry infrastructure is well-developed. These resonators are designed to have equispaced modes by confining light within a parabolic potential. This sample also contains a ring resonator, which allows us to compare with PhC cavity without drastically changing the experimental parameters. A typical spectrum of a PhC (focused on three resonances) is given in Fig. 6(a).

### 2. Pair generation measurement

#### *a. Thermal tuning*

Deviation from the triply resonant configuration can be compensated using thermal tuning. A pump laser (Keysight 8164B) is sent into the cavity at a fixed frequency $\omega_p$ close to the pump mode frequency $\bar{\omega}_0$. The temperature of the sample is decreased using a Peltier module driven by an external temperature controller (ILX Lightwave LDT-5545B) with 0.1 Â°C precision. This causes a spectral shift of the pump mode, allowing the laser to enter the resonance. Direct transmission of the sample is measured with a power meter (Thorlabs

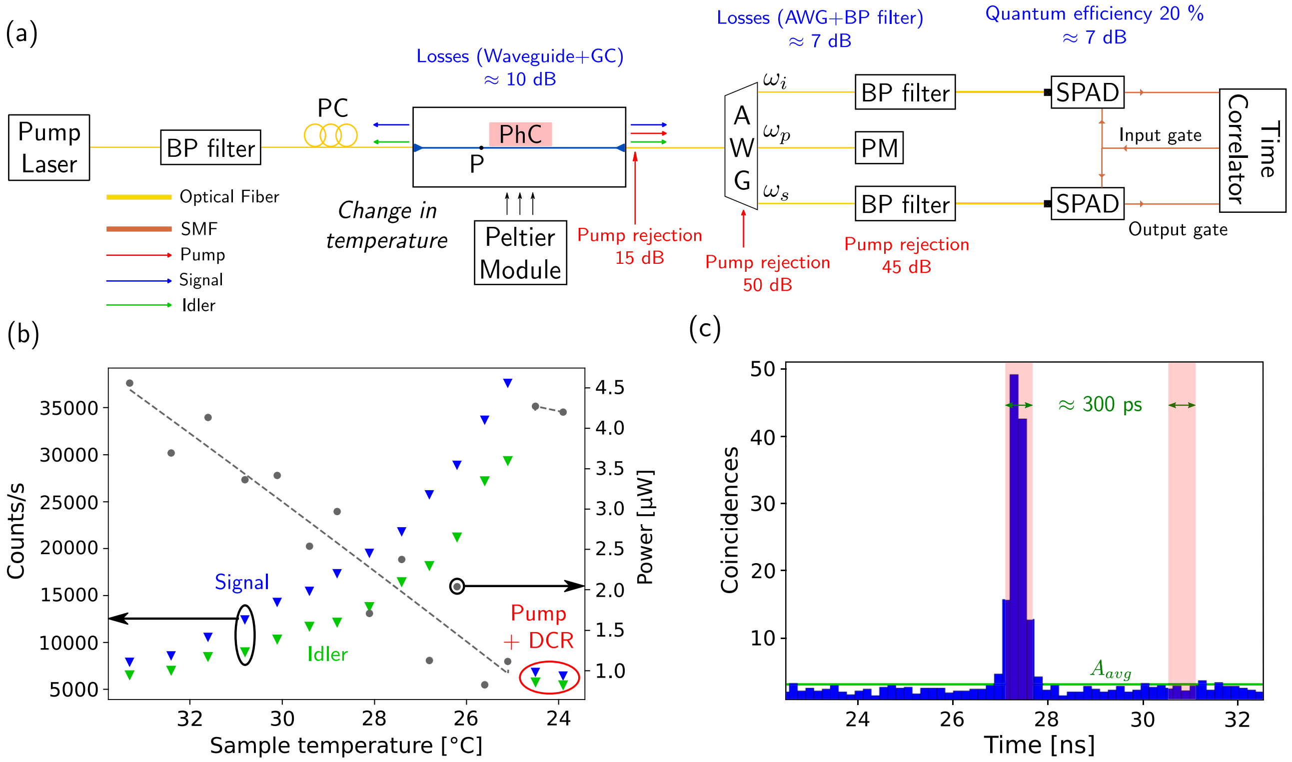

FIG. 7. Photon pair generation measurement. (a) Experimental setup. BP filter denotes band-pass filter, PC denotes polarization controller, P denotes on-chip power, GC denotes grating coupler, PM denotes power meter, and SPAD denotes single-photon avalanche photodiode. Losses encountered by the pump (red) and the signal/idler (blue) are detailed for each component. The time correlator generates the gating signal for the detectors. (b) Typical raw counts/0.1 s on each detector and transmitted pump power vs the temperature. DCR denotes dark count rate. (c) Typical histogram representing the main coincidence peak of ≈ 300 ps width (red rectangle) and the background average (green line). The second red rectangle far from the peak represents the integration window far from the peak to calculate the accidental counts $A$.

PM101-R) and shown in Fig. 2(a). The transmitted power drops, causing an increase in the intracavity energy $W$ due to absorption, until the bistable point where the laser is back out of resonance. Pump-probe optical coherent tomography (OCT) measurement [24] is performed for different temperatures to extract precisely the resonance frequencies. Each measurement for a given temperature corresponds to a value of the pump offset, which allows us to compare the experimental data to the model derived in Appendix A.

### *b. Operation of the detectors*

The single-photon avalanche photodiode (SPAD, Aurea Technology OEM-NIR) has been used with a quantum efficiency $\eta_q$ of 20% and a deadtime $\tau_D$ of 15 $\mu$s to compromise between losses reduction and false detected events such as afterpulsing or dark count rate (1000 counts/s in these conditions). The gating signal is directly generated by the time correlator (TC, Aurea Technology Chronoxea) with a fixed duty cycle $\sigma$ of 0.5. The frequency of the signal has been set to 3 MHz as a tradeoff between minimizing the accidental counts and reducing the afterpulsing probability (here $< 0.01$).

### *c. Single counts and pump attenuation*

As SPAD cannot discriminate between different wavelengths; it is necessary to reject residual pump photons after the cavity to limit accidental counts on the detectors. Typical pump attenuation values are given in Fig. 7(a). Attenuation is first due to the fall in transmission as the pump mode gets resonant (≈5 dB), then losses in the waveguide and the grating coupler to extract the light (≈10 dB). The filtering setup, combining DWDM (AFW technologies SM-D-16) and band-pass filters (Yenista XTM-50) centered at $\omega_s$ and $\omega_i$, provides a necessary additional suppression. However, the total attenuation level of 110 dB is not enough to totally cut the pump at the detectors. The single counts on each channel can be directly measured by the two SPAD and are given in Fig. 7(b) (for cavity $B$), showing the generation of signal/idler photons as the modes get closer to the TRC. However, a level of 5000 counts/s above the DCR (1000 counts/s) level is measured out of resonance, meaning residual pump power (a few fW) is still present. Total pump attenuation would be obtained if the pump power at the detectors is lower than the DCR level (here 1 fW). This is almost the case, but these residual counts cause CAR degradation.

### *d. Signal, idler losses*

Signal and idler photons encounter losses from the output of the cavity to the detectors, taking into account their quantum efficiency. They are estimated between 25 and 30 dB per channel. They are described in Fig. 7(a), to which must be added 3 dB as pairs can be emitted on both sides of the waveguide, but they are only collected on one output side.

Losses have been measured using a wide-band source and an optical spectrum analyzer (Yokogawa) to extract the different transmission spectra.

#### *e. On-chip and equivalent pump power*

The estimation of pump losses through the sample gives a relation between the injected power in the waveguide $P_{\text{in}}$ and the output measured power $P_{\text{out}}$ out of resonance. Assuming symmetrical coupling insertion losses and knowing that the cavity is at the center of the waveguide gives an estimation for the power at the input of cavity $P_{c,\text{in}}$:

$$P_{c,\text{in}} = \sqrt{P_{\text{in}} P_{\text{out}}}. \tag{B1}$$

To appreciate the scaling of the generation efficiency on the $Q$ factor, it is handy to redefine the pump power so as to account for the internal losses. In fact, Eq. (A10) tells us that, keeping $Q$ fixed, the maximum efficiency is maximized in the side-coupled configuration when $2\kappa_0 = \Gamma_0$. In other words, maximum efficiency is achieved when the mode in resonance with the pump has no internal losses. In this case, the same generation rate is achieved with lower pump power, namely

$$P_{\text{eq}} = \frac{2\kappa_0}{\Gamma_0} P_{c,\text{in}}. \tag{B2}$$

Proceeding similarly with ring resonators yields

$$P = \frac{\kappa}{\Gamma} P_{c,\text{in}}. \tag{B3}$$

#### *f. Data extraction from the histogram*

The histogram [Fig. 7(c)], acquired by the TC during $T_{\text{int}} = 180$ s, is composed of a main peak, corresponding to coincidences and a wide background distribution due to the accidental counts. The main peak has a rough width of 300 ps, which changes slightly between the different experiments. The full width at half-maximum of the peak is given by [27]

$$\sigma_t = \sqrt{\sigma_{\text{jitter}}^2 + \sigma_{\text{res}}^2 + \sigma_{\text{coh}}^2}, \tag{B4}$$

with $\sigma_{\text{res}} \approx 13$ ps being the time resolution of the TC, and $\sigma_{\text{coh}} \approx$ a few ps is the lifetime of the photon in the cavity ($Q \approx 30\,000$–$40\,000$). It is then limited by the timing jitter of the detectors, $\sigma_{\text{jitter}} \approx 150$ ps. The raw number of coincidences $C_{\text{raw}}$ is extracted by taking the maximum value of the histogram [red point in Fig. 7(c)] and adding the coincidences in each time bin up to 150 ps on each side of the peak. The number of accidental counts $A$ is calculated by averaging the background distribution [green line in Fig. 7(c)] and multiplying it by the number of time bins corresponding to 300 ps. The width of integration (300 ps) has been kept constant to keep the comparison consistent as the CAR depends on the temporal window width [21], despite losing some coincidences as the distribution width was increasing with higher coincidence rates. True coincidences $C_T = C_{\text{raw}} - A$ are calculated, and then a further correction taking into account the detector response (deadtime and duty cycle) gives a real number of coincidences on detectors $C$ [19,28],

$$C = \frac{C_T}{(1 - N_1\tau_D)(1 - N_2\tau_D)\sigma}. \tag{B5}$$

The coincidence rate is then given by $R_{\text{det}} = C/T_{\text{int}}$. The pair generation rate is then given by $R = \alpha_i\alpha_s R_{\text{det}}$, with $\alpha$ the attenuation on the signal and idler channel.

#### *g. Measurement errors on the pair generation rate*

The experimental error on the pair generation rate $R$ is calculated by measuring the errors on the attenuation on each channel ($s$ and $i$) and the coincidence rate $R_{\text{det}}$. As $R = \alpha_s\alpha_i R_{\text{det}}$, the error $\Delta R$ is given by

$$\frac{\Delta R}{R} = \sqrt{\left(\frac{\Delta\alpha_i}{\alpha_i}\right)^2 + \left(\frac{\Delta\alpha_s}{\alpha_s}\right)^2 + \left(\frac{\Delta R_{\text{det}}}{R_{\text{det}}}\right)^2}. \tag{B6}$$

Measurement error on $R_{\text{det}}$ is estimated with the measurement error on the raw number of coincidence $C_{\text{raw}}$ (Poisson distribution) [27], the accidental counts $A$ (being standard deviation of the distribution) and errors on average counts ($N_1$, $N_2$) on each detector, which correspond to the standard deviation of the distribution. Errors on the deadtime and the duty cycle are supposed to be negligible compared to the previous terms. Concerning the losses, relative error on the attenuation $\alpha$ (defined by a power ratio) is related to the relative error (measured in dBm) ($\Delta P$):

$$\frac{\Delta\alpha}{\alpha} \approx 0.23\sqrt{2}\Delta P. \tag{B7}$$

$\Delta P$ is taken as 0.1 dBm.

### 3. Pump-probe optical coherent tomography measurement

Optical coherent tomography (OCT) is an interferometric measurement used to measure either the transmission or the reflection spectra of a sample using a sweeping laser as the source. Resonances frequencies, quality factors (total damping rates $\Gamma_-, \Gamma_0, \Gamma_+$), and FSR can be extracted from this phase-sensitive measurement with Fourier analysis and an appropriate model [24].

To reveal the evolution with temperature of the triplet frequencies ($\omega_-$, $\omega_0$, $\omega_+$) when the cavity is pumped, pump-probe OCT measurement is performed [Fig. 8(a)]. In addition to the sweeping (probe) laser (Keysight 8164B), a pump laser (PurePhotonics PPCL200) at fixed angular frequency is injected in the cavity, and transmission spectra are measured for different temperatures. A 90/10 coupler is added at the end of the waveguide to directly measure the pump transmission with a power meter (Thorlabs-PM101R). To be consistent with the pair generation measurement, the same pump power must be injected on-chip, otherwise the bistable jump occurs at a different temperature. The measurement is based on optical homodyne detection, therefore it is not hampered by the pump, and the pump is contradirectional to the probe beam. First, the resonance shift $\Delta\omega_0 = \omega_0 - \bar{\omega}_0$ [Fig. 8(b)] (assimilated to the pump offset $\Delta_0$) is calculated, and its maximum value (just before the bistable) jump is by definition $\Delta_{\text{bist}}$. This requires us to calculate the cold cavity pump mode resonance $\bar{\omega}_0$, which is linearly fitted with the temperature using "out-of-resonance" points of $\omega_0$, thus it is unaffected by the pump laser [Fig. 2(b)]. Secondly [Fig. 8(c)], FSR are calculated and linearly fitted once the transmission starts to drop. The two curves cross at the triply resonant configuration, revealing the

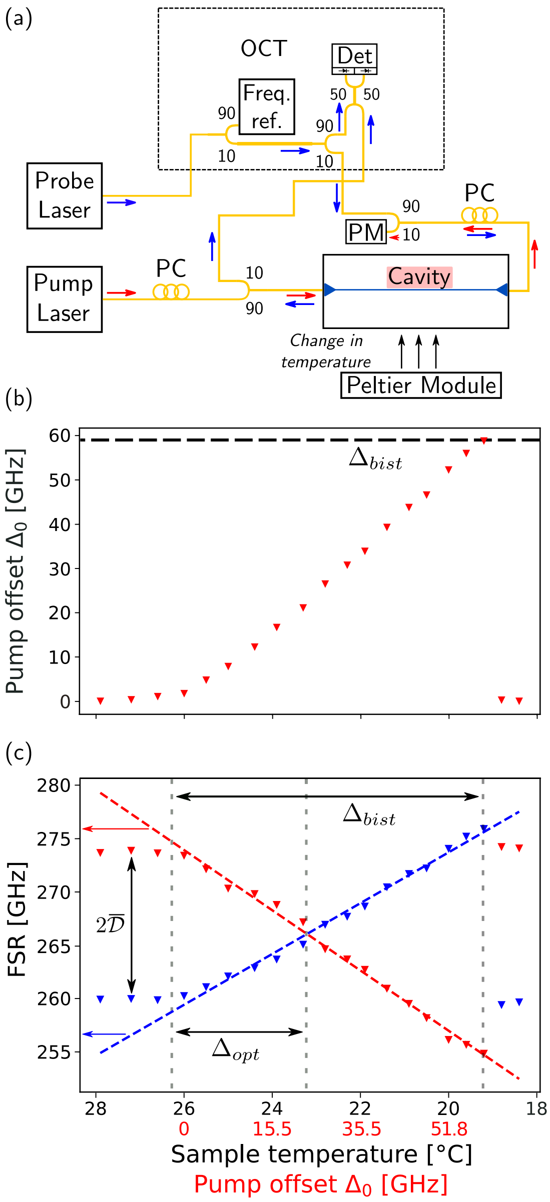

FIG. 8. Pump-probe OCT. (a) Experimental setup: PM, power meter; PC, polarization controller; Freq. Ref., reference interferometer; and Det., balanced photodiode (Thorlabs PDB450C). (b) Pump offset vs the temperature and extraction of $\Delta_{\text{bist}}$. (c) FSR (blue, red triangle) vs temperature and extraction of $\Delta_{\text{opt}}$ and $\bar{\Delta}_\chi$. The values of the pump offset displayed above the figure are calculated with (b).

value of $\Delta_{\text{opt}}$. Additionally, the initial frequency mismatch $\bar{\Delta}_\chi$ is also estimated by considering out-of-resonance points.

The values of $\Delta_{\text{opt}}$ and $\Delta_{\text{bist}}$ are limited by the number of temperature points. It is taken as the space between two points, namely 4 GHz. Measurement error on $\bar{\Delta}_\chi$ has been determined with a statistical study as it can be calculated for each "out-of-resonance" point [for example, five times in Fig. 8(c)].

### 4. Stimulated conversion efficiency

The maximum value of the stimulated conversion efficiency (SCE) $\eta_\chi^{\text{max}}$ is the last of the parameter to be assessed, with a CW pump-probe measurement. It is done by pumping the cavity with a laser (PurePhotonics PPCL200) at a fixed frequency $\omega_p$ and changing the temperature to scan the pump mode around the laser. Additionally, another laser (Keysight 8164B) is swept across the signal resonance to stimulate the process [Fig. 9(a)], with a power one order of magnitude lower than the pump. At the output of the waveguide is an optical spectrum analyzer (Yokogawa AQ6370D). Measuring the output idler power $P_{\text{id,out}}$, the output signal power out of resonance (which can be accounted as the incoming signal power) $P_{s,\text{in}}$, and the losses for each wavelength between the output of the cavity and the OSA gives an experimental value for $\eta_\chi$:

$$\eta_\chi = \frac{\alpha_s}{\alpha_i}\frac{P_{\text{id,out}}}{P_{s_in}}. \tag{B8}$$

For a given temperature (a given pump offset $\Delta_0$), a scan around the signal frequency reveals stimulated idler photons

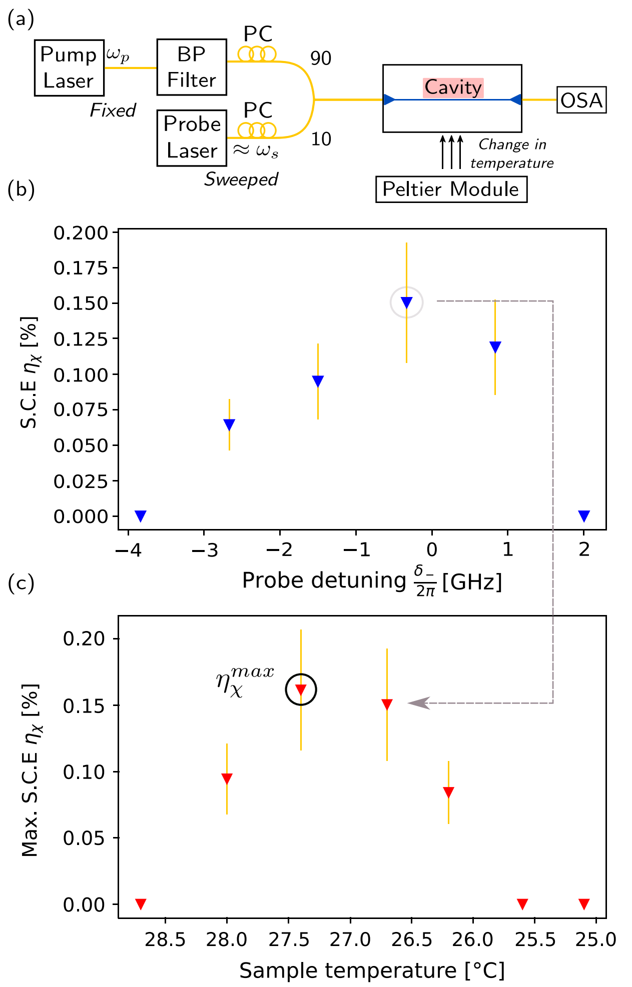

FIG. 9. Stimulated conversion efficiency measurement (SCE). (a) Experimental setup: PC, polarization controller; OSA, optical spectrum analyser. (b) SCE for different values of the probe detuning for a given temperature. (c) SCE vs temperature. These values correspond to the maximum value scanned with the probe laser around the signal wavelength as depicted by the gray arrow. Extraction of $\eta_\chi^{\text{max}}$ is done by taking the maximum value (black circle).

TABLE II. Measured model parameters.

| Parameter | Cavity *A* | Cavity *B* | Cavity *C* |
|---|---|---|---|
| l ($\mu$m) | 150 | 125 | 100 |
| w (nm) | 500 | 500 | 400 |
| $\alpha_i$ (dB) | $26.6 \pm 0.5$ | $27 \pm 0.5$ | $29 \pm 0.5$ |
| $\alpha_s$ (dB) | $26.5 \pm 0.5$ | $26.6 \pm 0.5$ | $27.5 \pm 0.5$ |
| $\Gamma_-$ (GHz) | $9.20 \pm 0.5$ | $9.12 \pm 0.5$ | $9.41 \pm 0.5$ |
| $\Gamma_0$ (GHz) | $4.60 \pm 0.5$ | $4.74 \pm 0.5$ | $4.90 \pm 0.5$ |
| $\Gamma_+$ (GHz) | $3.88 \pm 0.5$ | $3.8 \pm 0.5$ | $3.07 \pm 0.5$ |
| $\overline{\mathcal{D}}$ (GHz) | $-6.7 \pm 0.3$ | $-16.4 \pm 0.3$ | $-4 \pm 0.3$ |
| $\Delta_{\mathrm{opt}}$ (GHz) | $25 \pm 4$ | $64 \pm 4$ | $16 \pm 4$ |
| $\Delta_{\mathrm{bist}}$ (GHz) | $57 \pm 4$ | $69 \pm 4$ | $42 \pm 4$ |
| $\eta_\chi^{\max}$ (%) | $0.08 \pm 0.02$ | $0.13 \pm 0.03$ | $0.18 \pm 0.05$ |
| $R_{\max}$ (MHz) | $1.2 \pm 0.3$ | $5.2 \pm 0.5$ | $4.8 \pm 0.5$ |

shown in Fig. 9(b) for different probe (signal) detuning $\delta_- = \omega_s - \omega_-$. The maximum value is kept and the procedure is repeated for each temperature [Fig. 9(c)]. The maximum value in temperature (pump offset $\Delta_0$) is then extracted and corresponds to $\eta_\chi^{\max}$ following its definition and Eq. (A9). The measurement error calculation is similar to Eq. (B7), given by

$$\frac{\Delta\eta_\chi}{\eta_\chi} \approx 0.23\sqrt{6}\Delta P. \tag{B9}$$

## APPENDIX C: COMPARISON OF EXPERIMENTS WITH THE THEORY

### 1. PhC model and experiment comparison

Experiments have been performed on three different PhC cavities (*A*, *B*, and *C*) on the same chip with different geometrical parameters such as the cavity length $l$ and the width of the waveguide $w$. The pair generation rate and the model parameters (shown in Table II) have been measured, and a comparison is shown in Fig. 10. Theory (blue line) is calculated with Eq. (A16), and the parameters are measured as presented in the previous section. No fitting has been done.

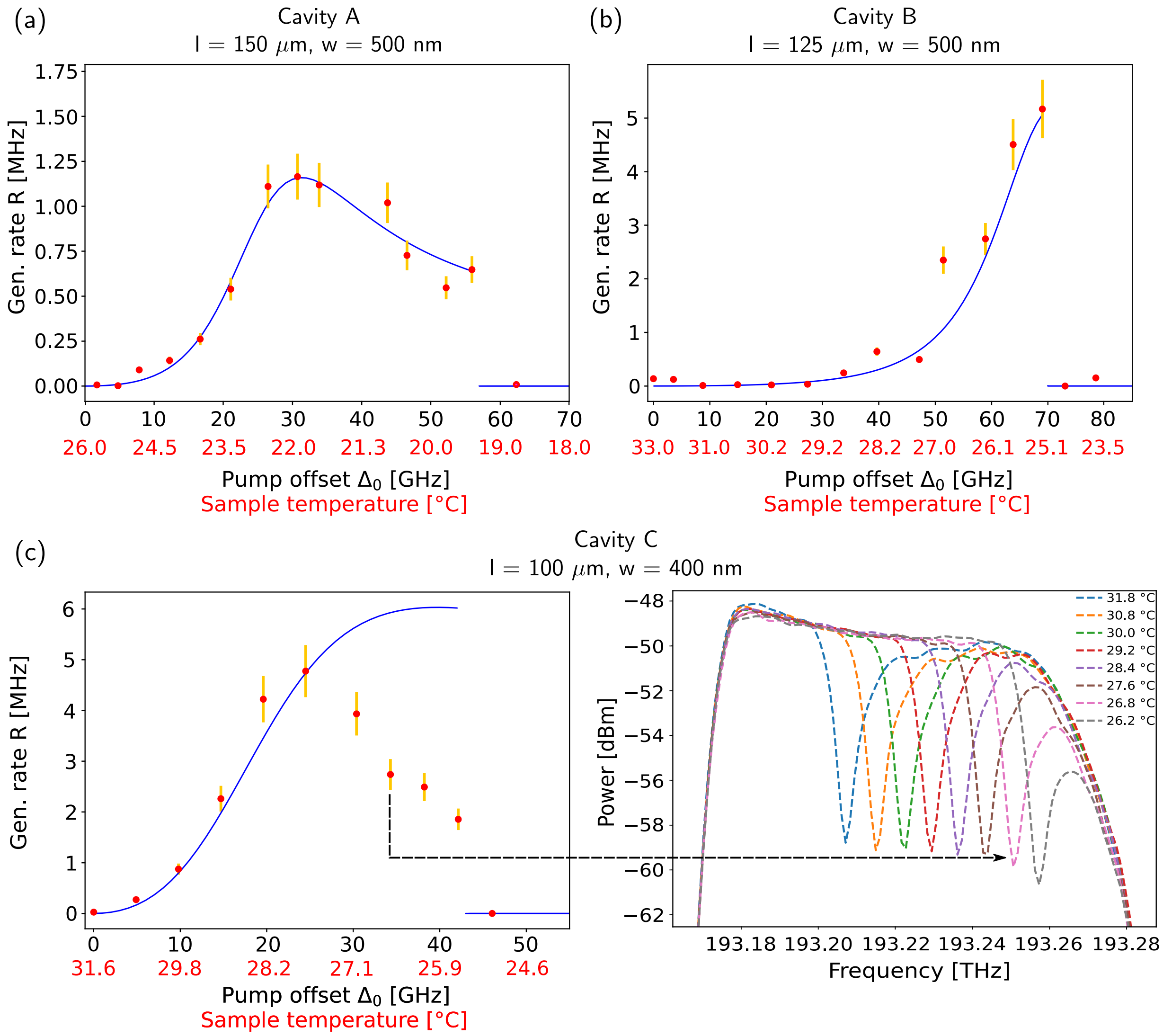

FIG. 10. Theory vs experiment pair generation rate for three different PhC cavities (red points, experiment; blue line, model). Parts (a), (b), and (c) correspond to cavity *A*, *B*, and *C*, respectively. The inset shows transmission spectra around a resonance for different temperatures. The resonance can gradually be shifted out of the transmission window of the filter, generating a drop in the pair generation rate.

The third PhC measurement (cavity $C$) has been impacted by temperature-dependent losses leading to a drop in $R$. First, spectral shift can gradually push the resonance out of the bandwidth of the filters (AWG + band-pass filter) and induce additional losses as depicted in the transmission spectra in the inset of Fig. 10(c). Secondly, for this waveguide width, FSR is around 500 GHz, which is wide enough to induce a different transmission through the output grating coupler. The expected maximum value has not been reached, which should have been the best observed rate (theoretically: roughly 6 MHz) because the volume for this cavity was the smallest (although lower quality) factors Table II.

As for the cavity $A$, a lower pair generation rate has been measured. Although the volume is bigger for this one, it does not completely explain this value. The pump modes of cavity $A$ and $B$ both roughly have the same linewidth (Table II). The lower value for $\Delta_{\text{bist}}$ for cavity $A$ shows that the bistable jump has not been pushed as far as for cavity $B$, highlighting that the pump resonance might not be well-coupled. This can result in an overestimation of the pump power really coupled to the cavity.

### 2. Measurements on a ring resonator

Measurements have been done on different ring resonators. The results presented here have been performed on a ring resonator of radius $r = 30\ \mu$m, width 600 nm, and comparable $Q$-factor with the PhCs. The width of the waveguide is also 500 nm [Fig. 11(a)]. Although no tuning mechanism is necessary as modes are roughly aligned as presented in a measured transmission spectra of one ring resonator [Fig. 11(b)], thermo-optic effects still have to be dealt with. For a given on-chip pump power, single counts on each detector are measured. They are maximum just before the bistable jump as the intracavity energy is maximum. At this operating point, a histogram was acquired during $T_{\text{int}}$, with the same experimental parameters, and the same post data treatment was applied to retrieve the generation rate $R$. The losses on each channel are 24.5 and 25 dB, which is consistent with PhC measurement without the additional 3 dB for emission on both sides of the waveguide (Table II). The quadratic scaling rule is recovered for the coincidence rate $R_{\text{det}}$ (as for $R$) as the decrease of the CAR with the increasing on-chip pump power [Fig. 11(c)].

### 3. Comparison between PhC ring resonator

The maximum value of the generation rate $R$ for each PhC cavity have been taken and compared with a ring resonator. This comparison highlighted the importance of the cavity volume. Our PhC cavity was able to confine light in a smaller volume than the ring resonator, leading to a better generation rate. To quantify this point, the nonlinear interaction volume $V_\chi$ has been calculated by taking into account the spatial overlap of the different waves in the cavity [16] and extrapolating these values for our PhC cavity. For the ring, $V_{\chi,\text{ring}} = 1.54 A_{\text{eff}} L$ [7], with $A_{\text{eff}}$ being the effective area of the cavity, and $L$ is its perimeter. Finally, the CAR has been calculated, showing that PhC can achieve decent CAR values with a better generation rate. Big error measurements on the curve can be explained by the acquisition time of the histogram, which was set to 180 s, which is consistent with a good coincidence rate, but it was not long enough to correctly fill all the bins in the accidental distribution. The standard deviation is bigger than the average accidental distribution, giving a big error on the accidental and corrected counts, thus on the CAR.

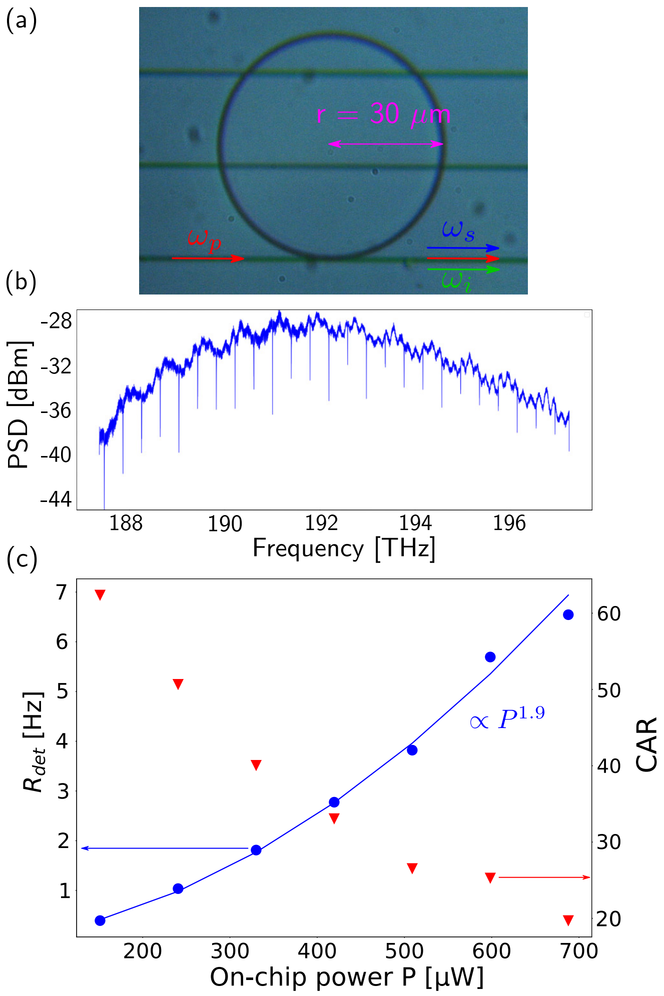

FIG. 11. Ring resonator study. (a) Picture of the ring resonator coupled to the waveguide. (b) Typical transmission spectrum of the ring resonator (PSD denotes power spectral density). (c) Pair generation rate (blue circles) and CAR (red triangle) vs on-chip pump power $P$. The polynomial fit (blue line) closely retrieves the quadratic scaling rule of $R$.

---

[1] P. G. Kwiat, K. Mattle, H. Weinfurter, A. Zeilinger, A. V. Sergienko, and Y. Shih, New High-Intensity Source of Polarization-Entangled Photon Pairs, Phys. Rev. Lett. **75**, 4337 (1995).

[2] D. Grassani, S. Azzini, M. Liscidini, M. Galli, M. J. Strain, M. Sorel, J. Sipe, and D. Bajoni, Micrometer-scale integrated silicon source of time-energy entangled photons, Optica **2**, 88 (2015).

[3] T. J. Steiner, J. E. Castro, L. Chang, Q. Dang, W. Xie, J. Norman, J. E. Bowers, and G. Moody, Ultrabright entangled-photon-pair generation from an AlGaAs-On-Insulator microring resonator, PRX Quantum **2**, 010337 (2021).

[4] Z. Ma, J.-Y. Chen, Z. Li, C. Tang, Y. M. Sua, H. Fan, and Y.-P. Huang, Ultrabright Quantum Photon Sources on Chip, Phys. Rev. Lett. **125**, 263602 (2020).

[5] M. Heuck, K. Jacobs, and D. R. Englund, Controlled-Phase Gate Using Dynamically Coupled Cavities and Optical Nonlinearities, Phys. Rev. Lett. **124**, 160501 (2020).

[6] S. Azzini, D. Grassani, M. J. Strain, M. Sorel, L. G. Helt, J. Sipe, M. Liscidini, M. Galli, and D. Bajoni, Ultra-low power generation of twin photons in a compact silicon ring resonator, Opt. Express **20**, 23100 (2012).

[7] G. Marty, S. Combrié, F. Raineri, and A. De Rossi, Photonic crystal optical parametric oscillator, Nat. Photon. **15**, 53 (2021).

[8] T. Asano, Y. Ochi, Y. Takahashi, K. Kishimoto, and S. Noda, Photonic crystal nanocavity with a $Q$ factor exceeding eleven million, Opt. Express **25**, 1769 (2017).

[9] S. Azzini, D. Grassani, M. Galli, D. Gerace, M. Patrini, M. Liscidini, P. Velha, and D. Bajoni, Stimulated and spontaneous four-wave mixing in silicon-on-insulator coupled photonic wire nano-cavities, Appl. Phys. Lett. **103**, 031117 (2013).

[10] C. Xiong, C. Monat, A. S. Clark, C. Grillet, G. D. Marshall, M. Steel, J. Li, L. OFaolain, T. F. Krauss, J. G. Rarity *et al.*, Slow-light enhanced correlated photon pair generation in a silicon photonic crystal waveguide, Opt. Lett. **36**, 3413 (2011).

[11] N. Matsuda, H. Takesue, K. Shimizu, Y. Tokura, E. Kuramochi, and M. Notomi, Slow light enhanced correlated photon pair generation in photonic-crystal coupled-resonator optical waveguides, Opt. Express **21**, 8596 (2013).

[12] A. Bazin, R. Raj, and F. Raineri, Design of silica encapsulated high-Q photonic crystal nanobeam cavity, J. Lightwave Technol. **32**, 952 (2013).

[13] S. Combrié, Q. V. Tran, A. De Rossi, C. Husko, and P. Colman, High quality GaInP nonlinear photonic crystals with minimized nonlinear absorption, Appl. Phys. Lett. **95**, 221108 (2009).

[14] P. Colman, C. Husko, S. Combrié, I. Sagnes, C. W. Wong, and A. De Rossi, Temporal solitons and pulse compression in photonic crystal waveguides, Nat. Photon. **4**, 862 (2010).

[15] I. Ghorbel, F. Swiadek, R. Zhu, D. Dolfi, G. Lehoucq, A. Martin, G. Moille, L. Morvan, R. Braive, S. Combrié, and A. De Rossi, Optomechanical gigahertz oscillator made of a two photon absorption free piezoelectric III/V semiconductor, APL Photon. **4**, 116103 (2019).

[16] G. Marty, S. Combrié, A. De Rossi, and F. Raineri, Hybrid InGaP nanobeam on silicon photonics for efficient four wave mixing, APL Photon. **4**, 120801 (2019).

[17] S. Sokolov, J. Lian, S. Combrié, A. De Rossi, and A. P. Mosk, Measurement of the linear thermo-optical coefficient of $Ga_{0.51}In_{0.49}P$ using photonic crystal nanocavities, Appl. Opt. **56**, 3219 (2017).

[18] K. Guo, E. N. Christensen, J. B. Christensen, J. G. Koefoed, D. Bacco, Y. Ding, H. Ou, and K. Rottwitt, High coincidence-to-accidental ratio continuous-wave photon-pair generation in a grating-coupled silicon strip waveguide, Appl. Phys. Express **10**, 062801 (2017).

[19] R. H. Hadfield, Single-photon detectors for optical quantum information applications, Nat. Photon. **3**, 696 (2009).

[20] M. Liscidini and J. E. Sipe, Stimulated Emission Tomography, Phys. Rev. Lett. **111**, 193602 (2013).

[21] E. Engin, D. Bonneau, C. M. Natarajan, A. S. Clark, M. G. Tanner, R. H. Hadfield, S. N. Dorenbos, V. Zwiller, K. Ohira, N. Suzuki *et al.*, Photon pair generation in a silicon micro-ring resonator with reverse bias enhancement, Opt. Express **21**, 27826 (2013).

[22] C. Ma, X. Wang, V. Anant, A. D. Beyer, M. D. Shaw, and S. Mookherjea, Silicon photonic entangled photon-pair and heralded single photon generation with CAR $> 12,000$ and $g^{(2)}(0) < 0.006$, Opt. Express **25**, 32995 (2017).

[23] R. R. Kumar, M. Raevskaia, V. Pogoretskii, Y. Jiao, and H. K. Tsang, Entangled photon pair generation from an inp membrane micro-ring resonator, Appl. Phys. Lett. **114**, 021104 (2019).

[24] S. Combrié, G. Lehoucq, G. Moille, A. Martin, and A. De Rossi, Comb of high-Q resonances in a compact photonic cavity, Laser Photon. Rev. **11**, 1700099 (2017).

[25] L. G. Helt, M. Liscidini, and J. E. Sipe, How does it scale? Comparing quantum and classical nonlinear optical processes in integrated devices, J. Opt. Soc. Am. B **29**, 2199 (2012).

[26] T. Carmon, L. Yang, and J. Vahala, Dynamical thermal behavior and thermal self-stability of microcavities, Opt. Express **12**, 4742 (2004).

[27] D. Oser, S. Tanzilli, F. Mazeas, C. Alonso-Ramos, X. Le Roux, G. Sauder, X. Hua, O. Alibart, L. Vivien, É. Cassan *et al.*, High-quality photonic entanglement out of a stand-alone silicon chip, npj Quantum Inf. **6**, 31 (2020).

[28] S. Rogers, X. Lu, W. C. Jiang, and Q. Lin, Twin photon pairs in a high-Q silicon microresonator, Appl. Phys. Lett. **107**, 041102 (2015).